Buried Interface Passivation of Perovskite Solar Cells by ALD Al_2O_3

Sudeshna Ghosh,[1] Debasmita Pariari,[2] Tejmani Behera,[3] Pablo P. Boix,[4] N. Ganesh,[5] Susmita Basak,[6] Arya Vidhan,[6] Nisha Sarda,[6] Iván Mora-Seró,[7] Arindam Chowdhury,[2] K. S. Narayan,[5] D. D. Sarma,[2,8*] and Shaibal K. Sarkar [6*]

[1] *Center for Research in Nanotechnology and Science, Indian Institute of Technology Bombay, Powai 400 076 Mumbai, India.*

[2] *Solid State and Structural Chemistry Unit, Indian Institute of Science, Bengaluru – 560012.*

[3] *Department of Chemistry, Indian Institute of Technology Bombay, Powai 400 076 Mumbai, India.*

[4] *Institut de Ciència dels Materials, University of Valencia Catedràtic J. Beltran 246980 Paterna, Valencia, Spain.*

[5] *Chemistry and Physics of Material Unit (CPMU), Jawaharlal Nehru Center for Advanced Scientific Research, Bengaluru 560064, India.*

[6] *Department of Energy Science and Engineering, Indian Institute of Technology Bombay, Powai 400 076 Mumbai, India.*

[7] *Institute of Advanced Materials, Universitat Jaume I, Av. de Vicent Sos Baynat, s/n 12071Castelló de la Plana, Spain.*

[8] *CSIR-National Institute for Interdisciplinary Science and Technology (CSIR-NIIST), Industrial Estate P.O., Pappanamcode, Thiruvananthapuram 695019, India.*

** Author for correspondence*

sarma@iisc.ac.in

shaibal.sarkar@iitb.ac.in

Abstract:

Despite of having long excited carrier lifetime and high mobility in halide perovskite material, the conventional (*n-i-p*) device witness significant interfacial non-radiative recombination losses that limits its radiative efficiency and consequently the overall open circuit potential. In this communication, we report that the process of spiro-OMeTAD coating on halide perovskite as a root-cause of such deleterious effect and we subsequently reveal a method to passivate these buried defect states by atomic layer deposition through a controlled precursor dosages on a fully functional device. The post device making Atomic Layer Deposition (ALD) process, results improvement of V_{OC} (~ 60-70 mV) and subsequently higher electroluminescence

quantum efficiency, and the overall device operational stability at maximum power point (MPPT).

Solar photovoltaic devices based on halide perovskite absorber have emerged to a point where commercialization can be expected in the near future[1]. Within a decade, the small area of single-junction perovskite devices has belligerently transpired from an encouraging 3.8%[2] to a contemporary value of 25.8%[3] suppressing its competitive third-generation photovoltaic technologies by far[4]. In addition to the material's apposite optoelectronic properties for the photovoltaic applications, the observed meteoric rise in the device efficiency should also be credited to a well-orchestrated rational development of the material and device processing methods[5]. With substantial improvements in the solution chemistry, bulk defects in the process-sensitive perovskite material are reduced as the estimated quasi-fermi level splitting (QFLS) in the bulk is near to the thermodynamic limit.[6] However, the polycrystalline nature of the material essentially induces large surface (or in-turn, interface) defect densities and promotes the non-radiative recombination losses which limit the open-circuit voltage (V_{OC}) deviating from its radiation limit[7]. In addition, very specific to the halide perovskite devices, the occurrence of a large density of the non-radiative recombination centers, which are essentially charged centers (when unoccupied) due to the mobile ionic species and hence contributes significantly in the local electronic band-structure, at the interface incubates the degradation processes and thus substantially reduces the overall device stability[8] [9]. Thus, for the overall development of the device, both in terms of efficiency and operational stability, the minimization of the non-radiative recombination centers at the surface is an essential step to be fulfilled.

As a major thrive to passivate the interfacial defects, many pathways are explored[10] [11]. Self-assembled monolayers at the base oxide materials (SnO_2[12] or TiO_2[13] for the *n-i-p* structures or NiO[14] for the *p-i-n* structure) and perovskite interface has proven to be one of the effective ways to minimize the interface defects. The use of a bi-functional molecular layer at the oxide-perovskite interface not only passivates the interfacial defects but the halide (or quasi-halide) termination helps the perovskite nucleation process[15]. In recent times, the incorporation of ionic liquids in the precursor solution have been an effective tool to passivate the interface and the grain boundaries, thus restricting the defect propagation[16]. In addition, the halide perovskite and hole transport layer (HTL) interface is specifically targeted by the 2D perovskite layers. The presence of the 2D (or even quasi-2D) structure not only passivated the interfacial defects but also provided chemical stability against the moisture ingress[17] [18] with a significant rise in the device parameters. However, the application of the low dimensional halide perovskite layer is yet to be rationalized and hence technological incubation on a larger scale is markedly difficult.

From the very early days of halide perovskite photovoltaics, atomic layer deposition (ALD) has been used as a tool to deposit either at ETL-perovskite[19] or HTL-perovskite[20] interface, aiming to reduce the interfacial recombination losses. ALD-grown oxide materials on ETL (*n-i-p* architecture) are more obvious choices either to cover the pin-holes of the solution-processed oxide materials or sometimes to provide a high dielectric layer to form a tunnel barrier[21]. In either of the scenarios, a controlled ALD layer is often proven to be beneficial as per the device parameters are concerned but pieces of evidence regarding either chemical or field-effect passivation is still largely lacking in the literature. However, due to the chemical incompatibility, ALD on perovskite is found to be more challenging and predictably induces the removal of the organic moiety from the surface[22] [23]. Despite that, several reports claim better device performances after the ALD-grown Al_2O_3 layer on the perovskite layers. Kausik et al.[24] have shown that a few cycles of Al_2O_3 on the methylammonium lead halide perovskite layer reduces the humidity-induced degradation as well as the hysteresis. However, we have previously shown that there is a preferential etching of the organic moiety by the metalorganic

precursors during the ALD process, leaving behind the PbI_2,[22] which is also subsequently reported by several other groups[23 25] through other in-situ measurements. However, whether the PbI_2 formation at the grain boundaries is found to be beneficial or not is still questionable[26] though preferred[27] but the uncontrolled formation of the same is unquestionably disadvantageous for the device performances.

In this communication, we introduce a post-device assembling process to reduce the non-radiative recombination at the buried interface in an (*n-i-p*) perovskite device employing Li-doped spiro-OMeTAD as an HTL. A substrate-enhanced ALD is employed on a full device that helps to passivate the HTL-perovskite interface with controlled PbI_2 formation. The process essentially improves the open circuit potential (V_{OC}) by ca. 70 mV resulting in a ca. 12% increment in the overall device efficiency and an order of magnitude improvement in the electroluminescence (EL) quantum yield. These improvements in the device parameters are found reproducible in similar device architecture (*n-i-p*) with different ETL (SnO_2 or TiO_2) and/or halide perovskite (methylammonium lead iodide or multication-multianion perovskite).

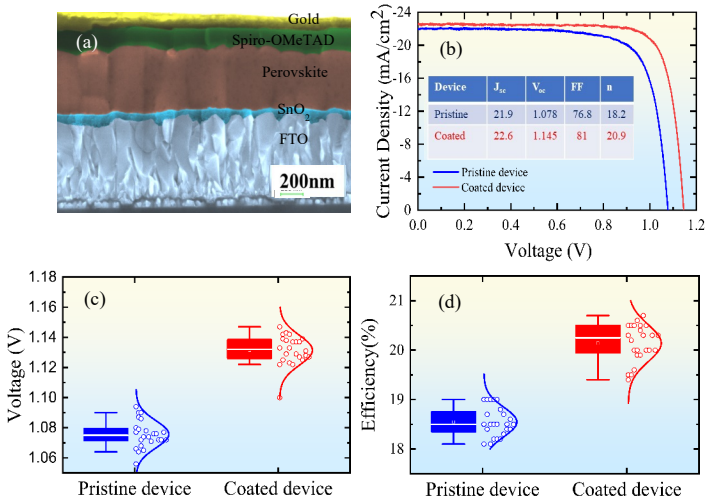

Figure 1. (a) Cross -sectional SEM image of FTO/Bi-layer SnO_2/Triple cation mixed halide perovskite/Spiro-OMeTAD/Au devices. (b) Light JV characteristics of Pristine and ALD -Al_2O_3 Coated perovskite photovoltaic devices in reverse scan direction (c) Statistical distribution of V_{OC} for Pristine and Coated devices (d) Statistical distribution of photoconversion efficiency for Pristine and Coated devices.

This investigation is based on the standard perovskite devices with *n-i-p* architecture with multi-cation multi-anion hybrid perovskite ($(FA_{0.83}MA_{0.17})_{0.95}Cs_{0.05}PbI_{2.5}Br_{0.5}$) as the absorber material, designated as *i*-layer, which is sandwiched between the carrier selective layers as shown in Figure 1a (cross section SEM image). For the electron transport layer (ETL), bi-layer SnO_2 (blocking and colloidal layer) is used while Li-TFSI doped spiro-OMeTAD is employed as the HTL. Standard device making protocols are used which is elaborated in the experimental section of SI. As-prepared device photoconversion efficiency lies in the range of 18-20% and for the purpose of this report we have not put much emphasis on device optimization. Al_2O_3

ALD coating on the as-prepared devices is conducted in a custom-built setup, explained elsewhere [1], at 70 ºC with alternate dosing of trimethyl aluminum (TMA) and H_2O. For the discussion below, it is worth mentioning here that since these devices (both, pristine and coated) do not show any measurable hysteresis (see Figure S1), thus for ease in illustration we show only the reverse *J-V* scans to represent the photovoltaic characteristics.

Figure 1b shows the current-voltage (*J-V*) characteristics, under illumination, of a representative device before (pristine) and after the ALD (coated device). As depicted, the ALD coating yields an increase of 67 mV in the V_{OC} resulting in an increment of the device efficiency from 18.2% to 20.9%, for the best performing devices as per the device efficiency value is concerned. Notably, the increase in the short-circuit current density (J_{SC}) is relatively slender, from 21.9 to 22.6 mA.cm^{-2} and so is the fill-factor (FF), from ~77% to 81%. Thus, the increase in the V_{OC} upon the ALD coating is majorly the responsible factor for the device efficiency enhancement. Figure 1c shows the statistical distribution of changes in the V_{OC} for 30 different devices. Here the change in the median of the distribution is ca. 55 mV resulting in a change in the device efficiency from 18.5% to 20.3% (median value) as shown in the Figure 1d**.** Corresponding, J_{SC} and FF values are also shown in Figures S2a and S2b, respectively. We need to clarify here, that considering the reproducibility in measurements, all the devices are measured with a shadow mask of an area of 0.03 cm^2 while the device active area is 0.12 cm^2. Thus, the recorded V_{OC}, reported here, is slightly lower than if otherwise measured under full device illumination. This is due to the persistent effect of the dark current contributed from the entire active area[28]. For one representative sample we found that the V_{OC} yields a value of 1.14 V for pristine and ~1.2 V for the coated one, as shown in Figure S3 under full illumination (i.e., without any shadow mask). Furthermore, to substantiate the aforementioned observation, a set of experiments are performed where the HTL and the ALD processes are kept invariant, but the underneath architecture is altered subsequently. With the same absorber layer, in the TiO_2-based device the absolute change in the efficiency after the ALD coating is 1.4%, see Figure S4a, while the overall improvement is ~2.1% when the multication perovskite is replaced with methylammonium lead iodide (MAPI), keeping SnO_2 as ETL, see Figure S4b. These results, even in unoptimized devices, suggest that the ETL-Perovskite interface has no major role to play in the enhancement of the overall device efficiency. Nevertheless, from the purist point of view, the thermal treatment during the course of the ALD process (70 ºC) cannot be ignored always as the perovskite material by itself is sensitive to the temperature. Our observations, however, reveal no significant behavioral changes in the device performances, before and after the specified thermal conditioning, and hence, ignored hereinafter.

To comprehend the enhancement of V_{OC} between the pristine and the Al_2O_3 coated devices, we performed steady-state photoluminescence (PL) studies, both microscopy (in a custom-built setup – see SI) and spectroscopy under open-circuit conditions. The room-temperature PL imaging and the spectra, shown in Figure S5 (and the discussion there), make it visibly obvious that the ALD coating enhances the PL intensity of the device without any noteworthy spectral shift. Considering the measurement conditions (both under steady-state and under open-circuit) and the fact that perovskite devices are primarily non-excitonic devices, the observed increase in the PL intensity upon ALD coating, therefore, corresponds to the larger quasi-Fermi level splitting (QFLS) and that in-turn resembling the higher V_{OC} that we observed. We need to keep in mind that there is little increase in the J_{SC} after the ALD coating. It is highly unlikely that the ALD Al_2O_3 coating on top of the device can influence the defect concentration in the bulk of the absorber material which is otherwise uniformly distributed throughout the thickness of the material. Such observations naturally lead to the assumption that the spatial location of the

non-radiative recombination centers arising from defects is dominated at the interface which is more likely to be affected by the ALD process. In order to probe the presence of defect states influencing the overall dynamics of charge carriers following the photoexcitation, we have carried out detailed time-resolved PL (TRPL) studies on the pristine and coated devices. Notably, for the ease of interpretation and considering the obvious assumption, explained previously, that the ALD process is unlikely to have any effect on the ETL or at the ETL-Perovskite interface, we used the half-cell configuration (i.e., without SnO_2) for the measurement. Signatures of the defect states in the PL spectra appear at longer wavelengths while the higher energy end is contributed by the bandgap emissions, but the broad PL spectra in Figure 2a do not allow a clear separation of these emissions arising from different origins. Therefore, we have carried out the TRPL studies at several photon energies that are marked in Figure 2a with yellow vertical lines. Therefore, observing the change in the decay life-time across the spectral width can give us important insight into the origins of de-excitation and therefore, on the presence of defect states. The PL intensity profile as a function of the delay time at each wavelength and its analysis are presented in the SI (Figure S6-S8 and Table S1-S3 and associated discussion). We found that all time-dependent PL intensity data for the coated sample can be reliably fitted with two time-scales, with a short life-time in the order of 2.25±0.004 ns contributing less than 10% of the total decay and a dominant one (> 90% of the decay) with a life-time of 17.74±0.211 ns, see Figure S6 and Table S1. Plots of the two lifetimes and their relative contributions as percentages of the total PL intensity are

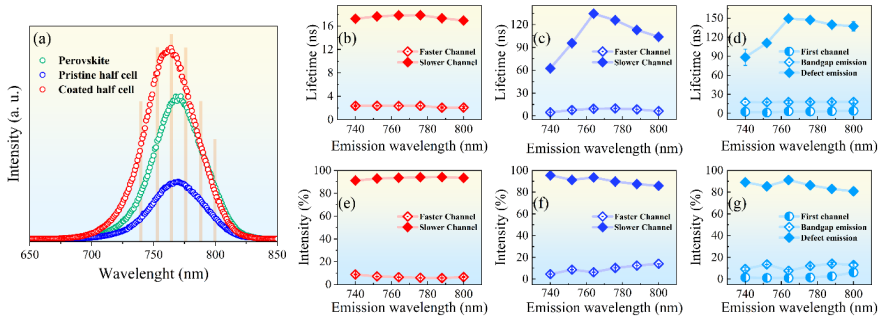

Figure 2. (a) Room temperature PL spectra collected on the Perovskite films and Pristine and ALD coated half-cells. The yellows lines are showing the emission wavelengths where lifetime are collected; Extracted lifetime as a function of emission wavelength from bi-exponential fitting for (b) Coated half-cell and (c) Pristine half-cell; (d) Extracted lifetime as a function of emission wavelength from tri-exponential fitting for pristine half-cell; Relative contributions of different decay channels as percentage of the total PL intensity for (e) Coated half-cell, (f) Pristine half cell (bi-exponential fitting) and (g) Pristine half cell (tri-exponential fitting).

shown as a function of the PL wavelength are shown in Figure 2b and 2c. The PL intensity decay for the pristine device could also be fitted with two life-times at each of the chosen wavelengths (see Figure S7 and Table S2) and the resulting life-times and relative contributions for the pristine device are shown in Figure 2d and 2e. Ignoring the minor contributions from the similarly short (~2 ns) life-time processes for both the samples, the remarkable difference in the life-time of the majority process is that it is essentially constant (~17.00±0.21 ns) independent of the wavelength for the coated sample, while it shows a systematic increase from a relatively low value of 35 ns at the shortest wavelength, reaching a highest value of 134 ns

and then decreasing more modestly to 104 ns, as a function of the wavelength. Such large values of the lifetime point to defect states being primarily responsible for these majority decay channel in the pristine sample. However, one would also expect overlapping contributions from the bandgap emissions in such samples as well. Motivated by this, we carried out a three-lifetime fitting of the PL decay plots of the pristine samples; while the details of the fitting and associated discussion are presented in the SI (see Figure S8 and Table S3), we show the results obtained in terms of the three life-times and their relative contributions as a function of the PL wavelength for the pristine sample in Figures 2f and 2g**.** This analysis clearly shows that there is indeed a bandgap emission with a shorter lifetime of ~17.00±0.21 ns that is essentially independent of the wavelength. This lifetime compares very well with the majority decay channel obtained for the coated sample, though the relative contribution of this bandgap emission channel drops from above 90% in the coated sample to ~11.7±2.4 % for the pristine sample. The majority of the decay in the pristine channel follows the longer decay time associated with overlapping defect states. These results clearly suggest that the ALD process to coat the device leads to a significant suppression of the defect states introduced at the level of preparing the pristine device, as discussed below.

A strong spectral overlap of the bandgap emission and the defect emission in the pristine sample at the room temperature does not allow identifications of the PL spectral contributions from these two channels, though the TRPL data, presented above, allow us a separation of their relative contributions. In order to identify spectrally resolved contributions from these two channels, we rely on a lower temperature (100 K) PL emission data obtained with a different spectrometer with higher spectral resolutions, shown in Figure 3a, where the temperature dependent shifts in PL originating from different channels help us see the defect emission as partially distinct from the bandgap emission. One obvious change that should be taken into the consideration is the ~20 nm red-shifted PL peak of the perovskite film appearing at ~770 nm in figure 2b when measured at 100 K against the same film measured at room-temperature with the PL peak at ~750 nm in Figure 3a. This shift is essentially due to the lattice contraction that results in a change in the bandgap as measured from the optical absorption spectra (refer to Figure S9 and the discussion there). Figure 3a clearly shows a shoulder in the PL spectra at ~785 nm, see Figure S10 for deconvoluted spectra, only for the pristine device sample and is absent for both the pristine perovskite and the coated device; in other words, this longer wavelength feature appears only after the spiro coating, suggesting that this step in the device construction introduces extensive defect states at the interface affecting the optoelectronic properties adversely. This is also indicated in Figure 3a showing that the PL intensity of the pristine perovskite is significantly reduced on making the pristine device with the spiro overlayer. Interestingly, upon ALD coating the PL signal associated with the defect states at ~785 nm is completely removed and there is a significant enhancement of the primary PL peak centered at ~770 nm. For the coated half-cell, another intriguing fact is the shape of the PL peak, in particular the full width at half maxima, FWHM ~15 nm, which is even lower than that of the pristine perovskite films, ~19 nm. Importantly, in the coated half-cell devices the high energy side of the peak coincide with the pristine perovskite material but the low energy end is slightly blue-shifted, which indicates the reduction of the intrinsic grain boundary defects in the perovskite materials, while the coated device appears to show dominantly the bandgap emission even at this lower temperature, consistent with our findings at the room temperature.

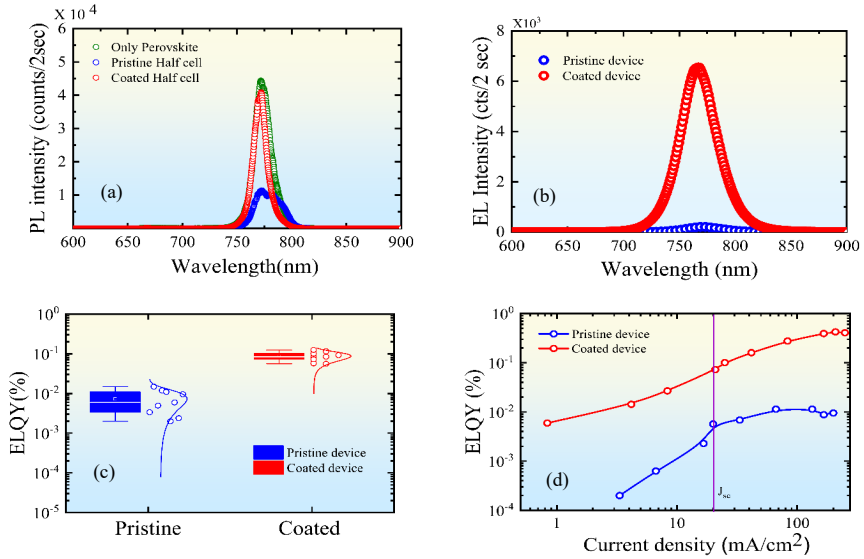

Figure 3. (a) PL spectra collected on the Perovskite films and Pristine and ALD coated half-cells at 100K. (b) Room temperature EL spectra collected on Pristine and Coated devices. (c) EL quantum yield (ELQY) collected on Pristine and Coated devices. (d) Variation in ELQY with injection current density measured on Pristine and Coated devices

To gain understanding on the correlation between the V_{OC} improvement and the radiative versus non-radiative recombination, we opted for electroluminescence (EL) measurements (spectroscopy and microscopy) of the same or similar devices before and after the ALD. As opposed to the PL measurements where the QFLS are induced by the absorbed photon, here the respective charge carriers are injected through the ETL and HTL resulting in the QFLS. However, in both scenarios (EL and PL), the magnitude of the signal quantifies the radiative recombination in the photoactive layer. Because of the charge injection dependency, the EL signal is more sensitive to the non-radiative centers at the interface. For our experiments, EL images and the corresponding spectra were taken, see SI for more details, with 1.2 V forward bias, as shown in Figure 3b. Notably here, a small but consistent blue shift (6 nm) is noted in the coated sample which is in concurrence with the previously reported observations[29] where such trends were used to suggest a lowered density of sub-bandgap states that mediate the non-radiative recombination. Most significantly, the EL intensity is found to be much higher for the coated device compared to the pristine device, once again proving the effective ALD-induced removal of the non-radiative defect centres that are generated after the spiro layer formation on top of the active material. In close agreement with Figure 3b, Figure 3c also reveals an enhancement of the EL quantum yield (ELQY) by approximately an order of magnitude. The ELQY is the ratio of the number of emitted photons to the net recombination (i.e., net charge carriers injected) which is measured at a constant current that is equal to the J_{SC}. ELQY in Figure 3c also shows approximately one order of magnitude in the coated device with respect to the pristine one. Such an improvement is in accord with our previous hypothesis

where the improved interface characteristics in the coated devices are found to be the key factor responsible for reducing the V_{OC} loss due to the nonradiative recombination, ΔV_{nr}, and pushing towards its radiative limit. This reduction of the voltage (ΔV_{nr}) can be quantitatively estimated by the reciprocity theorem[30] and mathematically expressed as

$$\Delta V_{nr} = -kT\, ln(ELQY) \qquad -- \qquad (1)$$

The above equation explicitly articulates the fact that higher ELQY corresponds to the lowered non-radiative losses. The average measured ELQY and the estimated ΔV_{nr} values of representative pristine and coated samples are presented in the table1. The coated devices are characterized by a reduced $\Delta V_{nr} \approx 176\, mV$. Furthermore, from the obtained ELQY values, the estimated difference in the voltage losses between the pristine and coated samples is ~ 62±7 mV which is in close agreement with the measured V_{OC} improvement (64 mV) in these devices, before and after the ALD coating. Thus, the EL measurements and analysis confirm that the ALD coating on the perovskite solar cells majorly suppresses the non-radiative pathways leading to considerably higher device performances. This is further confirmed by analyzing the ELQY at variable current densities. Figure 3d shows the ELQY for injection currents that was varied by approximately three orders of magnitude. The coated devices show EL switch-on characteristics even at relatively smaller currents in comparison to the pristine devices. Moreover, the ELQY is consistently higher by an order of magnitude across the range of the applied current densities. At higher current density (> 100 mA/cm^2), the efficiency roll-off is significantly reduced in the treated devices. This further confirms the significantly reduced non-radiative losses in the treated devices. The ELQY ~ 0.4 % at applied current density of 100 mA.cm^{-2}, which is comparable to previous observations in high-performance solar cell devices[31].

Device	ELQY (%)	-ΔVnr (mV)	Voc (V)
Pristine	0.007 ± 0.005	238 ± 18	1.078
Coated	0.0873 ± 0.023	176 ± 7	1.142
ΔV		62 ± 7	64 mV

Table 1: Percentage of EL quantum yield (ELQY) collected from Pristine and Coated devices and corresponding ΔVnr of Pristine and Coated device calculated using equation 1. From that ΔV (V_{oc} difference in both devices) is calculated which is close to experimental result.

We investigated the origin of this remarkable passivation of the buried perovskite-HTL interface from a fundamental standpoint, to decipher the role of ALD of Al_2O_3 in this process. The primary motivation of having Al_2O_3 ALD on the fully functional device is to achieve a thin film encapsulation [32] with an added advantage of low thermal budget due to the high exothermic reaction between TMA and H_2O. The relatively dense inorganic film with a low water vapor transmission rate is made to protect the devices from atmospheric water and oxygen[33]. However, the ALD process on organic material, spiro in the present case, is complex due to non-ideal surface termination or functionalization and inherent porosity. Here the nucleation process is more often substrate enhanced, unlike the surface-limited self-saturating displacement reaction. This is because the reactants, in particular TMA, infiltrates inside the bulk of the organic film[32] as schematically shown in Figures 4a and b. During the next half

ALD cycle, the deposition occurs from the bulk of the organic film. The depth of the formation of the inorganic film, Al_2O_3 here, depends on the diffusion properties (i.e., temperature, partial pressure, etc.) of both the reactants. We have previously shown[32] that the TMA settles well inside the spiro film with a low desorption rate during the first half cycle resulting in a significantly high mass loading unlike the second half cycle involving H_2O[32]. However, since the TMA is physiosorbed in the spiro film, the desorption kinetics also plays a significant role. Hence the purging time between the TMA and H_2O may play a major role in the deposition, as discussed later in the text. To reduce the dwelling time of the device at the elevated temperature and under a low vacuum, the purging time is generally reduced to an extent where the chemical vapor deposition (CVD) can be avoided. The purging time, in turn, depends on the pumping efficiency, which depends on the architecture of the ALD reactor. For the reactor involved in this work, we found that the 10 sec purging is just enough to drive the ALD reaction. Thus, with the combination of the low purge time and relatively lower infiltration of the H_2O molecule in the spiro layer the Al_2O_3 formation gets limited to the near-surface region of the spiro film. Most probably, the process leaves some unreacted TMA in the depth of the spiro films which reacts with the perovskite film at the interface as depicted in the Figure 4c and d. We have previously shown [22] that the TMA etches the perovskite film by reacting with the organic moiety of the hybrid structure and leaves behind PbI_2; the process alters the stoichiometry at the surface without any effect on the bulk of the material. Thus, the continuation of the repetitive process essentially promotes PbI_2 formation at the perovskite-spiro interface. Because of the consecutive reactant dosages during the ALD cycles, the volume adsorption of TMA gets subsequently lowered due to two factors; (a) increase in the hydroxy-terminated surface reactant sites and (b) a reduced chemical opacity due to the Al_2O_3 thin film growth at the surface. Thus, depending upon the dose parameters, the ALD process reaches the linear growth regime upon full surface coverage as schematically shown in Figure 4e. While looking from the ALD point of view, higher purging time between the consecutive dosages of chemicals allows the infiltrated TMA to diffuse out of the spiro layer due to the reversibility of the physisorption process. Under such deposition conditions, the V_{OC} improvement is negligible as shown in Figure S11. Considering these, we believe that there is further room for optimization that may lead to additional improvement; however, such optimization is beyond the scope and the aim of the present work.

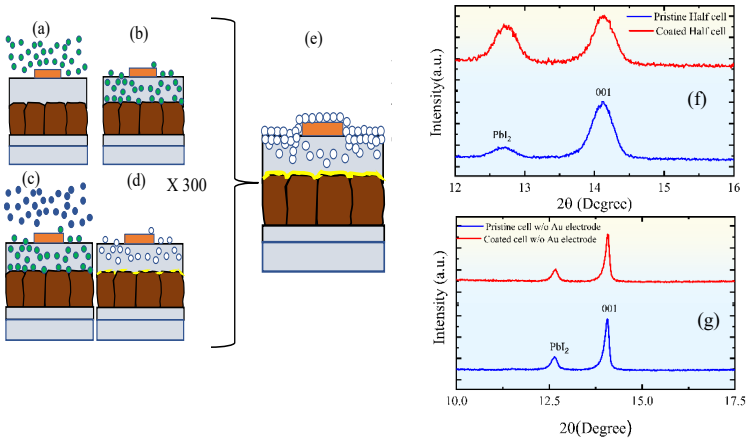

Figure 4. Schematic representation of ALD process is shown where (a) and (b) represent infiltration of TMA (Green circle) inside spiro in first half cycle. (c) Next half cycle demonstrates H_2O molecule's (Blue) reaction mechanism on device. (d) Representation of formation of Al_2O_3 (white circle) on devices after 300 cycles. (e) A Schematic representation depicts PbI_2 formation across perovskite spiro interface. (f) Grazing incidence XRD obtained from Pristine and Coated half cell (g) XRD (Brag-Brentano mode) of a full Pristine device (without the Au electrode) before and after the ALD Al_2O_3 coating.

To validate the PbI_2 formation at the interface due to the ALD process, we have performed x-ray diffraction (XRD) studies both under grazing angle (0.5° incidence) and Brag-Brentano (θ-2θ) mode of a full device (without the Au electrode) before and after the ALD Al_2O_3 coating, as shown in Figure 4f and g. Understandably, the grazing angle XRD reveals mostly the surface information while the data collected from the θ-2θ scan will be signatory of the volume of the material. The enhancement of the PbI_2 peak intensity ([001] plane at 2θ = 12.7°) can only be seen from the grazing angle diffraction pattern while no significant changes are obtained from the θ-2θ scan. The XRD analysis indicates that the ALD coating has not impacted any bulk properties, as per the crystal structure is concerned, of the perovskite while the interface is chemically modified with the formation PbI_2 only. A similar conclusion is drawn when the comparable devices are subjected to the TMA exposure only where the enhancement of the PbI_2 peak is duly noted as described in the Figure S12 but the Al_2O_3 formation due to the binary (TMA+H_2O) dosages provides additional device stability we also reported earlier[32].

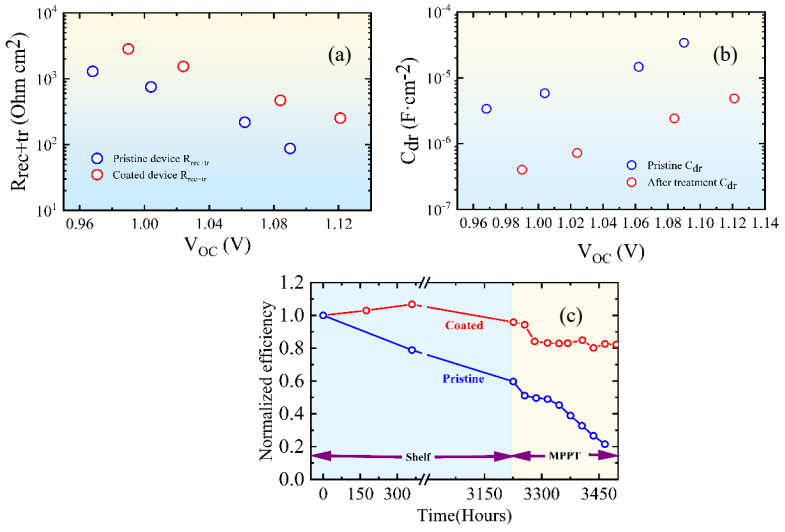

Figure 5. (a) Variation in R_{rec+tr} in Pristine (Blue) and Coated (Red) devices (b) C_{dr} variation in Pristine (Blue) and Coated (Red) devices (c) Stability test of Pristine and Coated devices where blue region is showing shelf-stability and yellow region is showing MPPT condition under 1 Sun illumination.

To bridge the understanding between the devices' optoelectronic properties and the PbI_2 formation at the interface, we measured electrochemical impedance spectroscopy (EIS) to identify the changes in the interfacial electronic properties of the coated versus pristine devices.

Comentado [IMS1]: Use Rrec and not Rrec+tr as the transport resistance is small in good performing devices (as the ones here) in comparison with the transport resistance

The capacitance characteristics measured in dark conditions display an order of magnitude reduction, primary in the low frequency values (0.01Hz), after the coating. This is attributed to the reduction in the electrode polarization, an essentially indication of a lowered ionic accumulation at the perovskite-HTL interface. EIS spectra are also recorded under illumination (with varied intensity) while keeping the device under the open-circuit condition. This enables the exploration of different charge concentration conditions as the photogenerated carriers are forced to recombine within the active layer. The Nyquist plots reproduced the typical two arcs of perovskite solar cells and were fitted with the equivalent circuit reported elsewhere [34] (see, Figure S13), to extract the relevant parameters. As depicted in Figure S13, the circuit contains three branches in parallel. One branch with the recombination resistance (R_{rec}), considering the transport resistance, negligible in the analyzed samples in comparison with the recombination resistance. Another parallel branch of the circuit contains one a capacitor (C_g) which represents the geometrical capacitance corresponding to the device's dielectric behavior, and the third branch includes a resistor (R_{dr}) in series with a capacitor (C_{dr}), which account for the ionic effects characteristic of perovskite solar cells and do not contribute at DC conditions. To account for small dispersion deviations, all the capacitors were modelled with constant phase elements keeping the exponents close to unity. While C_g does not present significant differences (Figure S14a), pointing towards a similar device thickness and overall dielectric properties, the coated sample shows larger R_{rec} values in Figure 5a. Given the good *FF* for both samples and the better V_{oc} of the coated sample, this R_{rec} difference is fully attributed to a recombination rate reduction, which origin can be related to a passivated PbI_2-rich interface in the Al_2O_3-coated sample. It has been previously demonstrated that small amounts of PbI_2 in perovskite devices can passivate the grain boundaries and promote the charge transport[27] [26]. Combining our observations, we can conclude that the formation of the PbI_2 at the perovskite-HTL interface, caused by the infiltration of TMA through the HTL layer in the ALD step of the device formation, reduces the interfacial recombination and renders better device V_{OC}. The Al_2O_3 encapsulation process also plays a role in the low frequency branch under illumination, with a slight increase of R_{dr} (Figure S11b), particularly evident at higher charge carrier concentration conditions, and a significant decrease of C_{dr} across the whole voltage range (Figure 5b). These observations indicate a reduction of the ionic concentration after the ALD treatment, in line with recent drift-diffusion simulations indicating that R_{dr} is not significantly affected by the ionic diffusion coefficient but by the ionic concentration[35]. The reduction of C_{dr}, in contrast, indicates an increase in the ionic mobility. Thus, these results can be interpreted in terms of a reduced ionic intercalation within the surface, as this interface becomes PbI_2-rich in the ALD-coated samples. In contrast, if the mobility of the surface-accumulated ions for the pristine devices is lower but they find a less ionic populated interface, then the build-up of carriers across the interface can also trigger higher interfacial recombination velocity, resulting in higher loss rate constants and reducing the device V_{OC}. The additive effects of reduced electrode polarization and reduced interfacial defects result an improvement of the overall device stability. Figure 5c shows a comparative performance of the device stability of a representative coated (red) and pristine (blue) device. These devices are subjected to the shelf stability and maximum power point tracking (MPPT), both under ambient condition. For the shelf-stability, the coated device retains 95% of its original efficiency after 3200 hrs. while for the pristine device it is ca. 60% (refer to the blue shaded section of Figure 5c). Under the MPPT condition, the coated devices are found highly stable after the initial burn-in period and constantly operated for ~ 300 hrs. at 90% of its starting efficiency while in comparison the pristine device dies down as clearly depicted in the Figure 5c (yellow shaded region).

In summary, we have demonstrated that the process of spiro-OMeTAD coating induces a significant defect at the interface resulting non-radiative recombination pathways. We have

Comentado [IMS2]: Add reference 34

categorically identified the contribution of these defect states in the overall excited carrier dynamics. Considering the fact that the TMA etches out the organic moiety from the hybrid perovskite and the diffusivity of the reactants through the organic charge transport layer is understandable, we employed the ALD Al_2O_3 coating which passivates the buried interface in a controlled manner by forming the PbI_2. While the detailed parametric analysis is not shown here but unarguably higher PbI_2 formation forms a charge transport barrier and certainly an unwanted scenario from the device point of view. The formation of the PbI_2 at the buried HTL-Perovskite interface results in the effective removal of the nonradiative recombination centers and as a consequence, the PL and ELQY get improved and hence the V_{OC} of the devices get improved by 60-70 mV. The proposed strategy is found simplistic and effective pathway to improve not only the overall device efficiency but also the operational stability as discussed here.

Acknowledgement:

Authors thank Ministry of New and Renewable Energy (MNRE), Govt. of India for financial support. S.K.S. and D.D.S. thank Department of Science and Technology (DST), Govt. of India for financial support through bilateral research grant. S.G., thanks University Grant Commission, T.B., D.P., S.B., thank Council of Scientific and Industrial Research, N.S. thanks Prime Minister Research Fellowship for student fellowship.

References:

(1) Cheng, Y.; Ding, L. Pushing commercialization of perovskite solar cells by improving their intrinsic stability. *Energy & Environmental Science* **2021**, *14* (6), 3233-3255, 10.1039/D1EE00493J. DOI: 10.1039/D1EE00493J.
(2) Kojima, A.; Teshima, K.; Shirai, Y.; Miyasaka, T. Organometal Halide Perovskites as Visible-Light Sensitizers for Photovoltaic Cells. *Journal of the American Chemical Society* **2009**, *131* (17), 6050-6051. DOI: 10.1021/ja809598r.
(3) Min, H.; Lee, D. Y.; Kim, J.; Kim, G.; Lee, K. S.; Kim, J.; Paik, M. J.; Kim, Y. K.; Kim, K. S.; Kim, M. G.; et al. Perovskite solar cells with atomically coherent interlayers on SnO2 electrodes. *Nature* **2021**, *598* (7881), 444-450. DOI: 10.1038/s41586-021-03964-8.
(4) Green, M. A.; Dunlop, E. D.; Hohl-Ebinger, J.; Yoshita, M.; Kopidakis, N.; Hao, X. Solar cell efficiency tables (version 59). *Progress in Photovoltaics: Research and Applications* **2022**, *30* (1), 3-12. DOI: https://doi.org/10.1002/pip.3506.
(5) Lee, D.-K.; Park, N.-G. Materials and Methods for High-Efficiency Perovskite Solar Modules. *Solar RRL* **2022**, *6* (3), 2100455. DOI: https://doi.org/10.1002/solr.202100455.
(6) Stolterfoht, M.; Caprioglio, P.; Wolff, C. M.; Márquez, J. A.; Nordmann, J.; Zhang, S.; Rothhardt, D.; Hörmann, U.; Amir, Y.; Redinger, A.; et al. The impact of energy alignment and interfacial recombination on the internal and external open-circuit voltage of perovskite solar cells. *Energy & Environmental Science* **2019**, *12* (9), 2778-2788, 10.1039/C9EE02020A. DOI: 10.1039/C9EE02020A.
(7) Oliver, R. D. J.; Caprioglio, P.; Peña-Camargo, F.; Buizza, L. R. V.; Zu, F.; Ramadan, A. J.; Motti, S. G.; Mahesh, S.; McCarthy, M. M.; Warby, J. H.; et al. Understanding and suppressing non-radiative losses in methylammonium-free wide-bandgap perovskite solar cells. *Energy & Environmental Science* **2022**, *15* (2), 714-726, 10.1039/D1EE02650J. DOI: 10.1039/D1EE02650J.

(8) Wolff, C. M.; Caprioglio, P.; Stolterfoht, M.; Neher, D. Nonradiative Recombination in Perovskite Solar Cells: The Role of Interfaces. *Advanced Materials* **2019**, *31* (52), 1902762. DOI: https://doi.org/10.1002/adma.201902762.
(9) Tress, W. Perovskite Solar Cells on the Way to Their Radiative Efficiency Limit – Insights Into a Success Story of High Open-Circuit Voltage and Low Recombination. *Advanced Energy Materials* **2017**, *7* (14), 1602358. DOI: https://doi.org/10.1002/aenm.201602358.
(10) Zhao, R.; Xie, L.; Zhuang, R.; Wu, T.; Zhao, R.; Wang, L.; Sun, L.; Hua, Y. Interfacial Defect Passivation and Charge Carrier Management for Efficient Perovskite Solar Cells via a Highly Crystalline Small Molecule. *ACS Energy Letters* **2021**, *6* (12), 4209-4219. DOI: 10.1021/acsenergylett.1c01898.
(11) Gao, F.; Zhao, Y.; Zhang, X.; You, J. Recent Progresses on Defect Passivation toward Efficient Perovskite Solar Cells. *Advanced Energy Materials* **2020**, *10* (13), 1902650. DOI: https://doi.org/10.1002/aenm.201902650.
(12) Kim, S. Y.; Cho, S. J.; Byeon, S. E.; He, X.; Yoon, H. J. Self-Assembled Monolayers as Interface Engineering Nanomaterials in Perovskite Solar Cells. *Advanced Energy Materials* **2020**, *10* (44), 2002606. DOI: https://doi.org/10.1002/aenm.202002606.
(13) Ali, F.; Roldán-Carmona, C.; Sohail, M.; Nazeeruddin, M. K. Applications of Self-Assembled Monolayers for Perovskite Solar Cells Interface Engineering to Address Efficiency and Stability. *Advanced Energy Materials* **2020**, *10* (48), 2002989. DOI: https://doi.org/10.1002/aenm.202002989.
(14) Phung, N.; Verheijen, M.; Todinova, A.; Datta, K.; Verhage, M.; Al-Ashouri, A.; Köbler, H.; Li, X.; Abate, A.; Albrecht, S.; et al. Enhanced Self-Assembled Monolayer Surface Coverage by ALD NiO in p-i-n Perovskite Solar Cells. *ACS Applied Materials & Interfaces* **2022**, *14* (1), 2166-2176. DOI: 10.1021/acsami.1c15860.
(15) Zhang, J.; Yang, J.; Dai, R.; Sheng, W.; Su, Y.; Zhong, Y.; Li, X.; Tan, L.; Chen, Y. Elimination of Interfacial Lattice Mismatch and Detrimental Reaction by Self-Assembled Layer Dual-Passivation for Efficient and Stable Inverted Perovskite Solar Cells. *Advanced Energy Materials* **2022**, *12* (18), 2103674. DOI: https://doi.org/10.1002/aenm.202103674.
(16) Lin, Y.-H.; Sakai, N.; Da, P.; Wu, J.; Sansom, H. C.; Ramadan, A. J.; Mahesh, S.; Liu, J.; Oliver, R. D. J.; Lim, J.; et al. A piperidinium salt stabilizes efficient metal-halide perovskite solar cells. *Science* **2020**, *369* (6499), 96-102. DOI: doi:10.1126/science.aba1628.
(17) Azmi, R.; Ugur, E.; Seitkhan, A.; Aljamaan, F.; Subbiah, A. S.; Liu, J.; Harrison, G. T.; Nugraha, M. I.; Eswaran, M. K.; Babics, M.; et al. Damp heat–stable perovskite solar cells with tailored-dimensionality 2D/3D heterojunctions. *Science* **2022**, *376* (6588), 73-77. DOI: doi:10.1126/science.abm5784.
(18) Mahmud, M. A.; Duong, T.; Peng, J.; Wu, Y.; Shen, H.; Walter, D.; Nguyen, H. T.; Mozaffari, N.; Tabi, G. D.; Catchpole, K. R.; et al. Origin of Efficiency and Stability Enhancement in High-Performing Mixed Dimensional 2D-3D Perovskite Solar Cells: A Review. *Advanced Functional Materials* **2022**, *32* (3), 2009164. DOI: https://doi.org/10.1002/adfm.202009164.
(19) Palmstrom, A. F.; Raiford, J. A.; Prasanna, R.; Bush, K. A.; Sponseller, M.; Cheacharoen, R.; Minichetti, M. C.; Bergsman, D. S.; Leijtens, T.; Wang, H.-P.; et al. Interfacial Effects of Tin Oxide Atomic Layer Deposition in Metal Halide Perovskite Photovoltaics. *Advanced Energy Materials* **2018**, *8* (23), 1800591, https://doi.org/10.1002/aenm.201800591. DOI: https://doi.org/10.1002/aenm.201800591 (acccessed 2022/07/02).
(20) Das, C.; Kot, M.; Hellmann, T.; Wittich, C.; Mankel, E.; Zimmermann, I.; Schmeisser, D.; Khaja Nazeeruddin, M.; Jaegermann, W. Atomic Layer-Deposited Aluminum Oxide Hinders

Iodide Migration and Stabilizes Perovskite Solar Cells. *Cell Reports Physical Science* **2020**, *1* (7), 100112. DOI: https://doi.org/10.1016/j.xcrp.2020.100112.
(21) Seo, S.; Jeong, S.; Park, H.; Shin, H.; Park, N.-G. Atomic layer deposition for efficient and stable perovskite solar cells. *Chemical Communications* **2019**, *55* (17), 2403-2416, 10.1039/C8CC09578G. DOI: 10.1039/C8CC09578G.
(22) Choudhury, D.; Rajaraman, G.; Sarkar, S. K. Self limiting atomic layer deposition of Al2O3 on perovskite surfaces: a reality? *Nanoscale* **2016**, *8* (14), 7459-7465, 10.1039/C5NR06974B. DOI: 10.1039/C5NR06974B.
(23) Koushik, D.; Hazendonk, L.; Zardetto, V.; Vandalon, V.; Verheijen, M. A.; Kessels, W. M. M.; Creatore, M. Chemical Analysis of the Interface between Hybrid Organic–Inorganic Perovskite and Atomic Layer Deposited Al2O3. *ACS Applied Materials & Interfaces* **2019**, *11* (5), 5526-5535. DOI: 10.1021/acsami.8b18307.
(24) Koushik, D.; Verhees, W. J. H.; Kuang, Y.; Veenstra, S.; Zhang, D.; Verheijen, M. A.; Creatore, M.; Schropp, R. E. I. High-efficiency humidity-stable planar perovskite solar cells based on atomic layer architecture. *Energy & Environmental Science* **2017**, *10* (1), 91-100, 10.1039/C6EE02687G. DOI: 10.1039/C6EE02687G.
(25) Petit, R. R.; Li, J.; Van de Voorde, B.; Van Vlierberghe, S.; Smet, P. F.; Detavernier, C. Atomic Layer Deposition on Polymer Thin Films: On the Role of Precursor Infiltration and Reactivity. *ACS Applied Materials & Interfaces* **2021**, *13* (38), 46151-46163. DOI: 10.1021/acsami.1c12933.
(26) Liu, F.; Dong, Q.; Wong, M. K.; Djurišić, A. B.; Ng, A.; Ren, Z.; Shen, Q.; Surya, C.; Chan, W. K.; Wang, J.; et al. Is Excess PbI2 Beneficial for Perovskite Solar Cell Performance? *Advanced Energy Materials* **2016**, *6* (7), 1502206. DOI: https://doi.org/10.1002/aenm.201502206.
(27) Chen, Q.; Zhou, H.; Song, T.-B.; Luo, S.; Hong, Z.; Duan, H.-S.; Dou, L.; Liu, Y.; Yang, Y. Controllable Self-Induced Passivation of Hybrid Lead Iodide Perovskites toward High Performance Solar Cells. *Nano Letters* **2014**, *14* (7), 4158-4163. DOI: 10.1021/nl501838y.
(28) Kiermasch, D.; Gil-Escrig, L.; Bolink, H. J.; Tvingstedt, K. Effects of Masking on Open-Circuit Voltage and Fill Factor in Solar Cells. *Joule* **2019**, *3* (1), 16-26. DOI: https://doi.org/10.1016/j.joule.2018.10.016.
(29) Yu, H.; Wang, H.; Zhang, T.; Yi, C.; Zheng, G.; Yin, C.; Karlsson, M.; Qin, J.; Wang, J.; Liu, X.-K.; et al. Color-Stable Blue Light-Emitting Diodes Enabled by Effective Passivation of Mixed Halide Perovskites. *The Journal of Physical Chemistry Letters* **2021**, *12* (26), 6041-6047. DOI: 10.1021/acs.jpclett.1c01547.
(30) Rau, U. Reciprocity relation between photovoltaic quantum efficiency and electroluminescent emission of solar cells. *Physical Review B* **2007**, *76* (8), 085303. DOI: 10.1103/PhysRevB.76.085303.
(31) Rai, M.; Wong, L. H.; Etgar, L. Effect of Perovskite Thickness on Electroluminescence and Solar Cell Conversion Efficiency. *The Journal of Physical Chemistry Letters* **2020**, *11* (19), 8189-8194. DOI: 10.1021/acs.jpclett.0c02363.
(32) Singh, R.; Ghosh, S.; Subbiah, A. S.; Mahuli, N.; Sarkar, S. K. ALD Al2O3 on hybrid perovskite solar cells: Unveiling the growth mechanism and long-term stability. *Solar Energy Materials and Solar Cells* **2020**, *205*, 110289. DOI: https://doi.org/10.1016/j.solmat.2019.110289.
(33) Ghosh, S.; Singh, R.; Subbiah, A. S.; Boix, P. P.; Seró, I. M.; Sarkar, S. K. Enhanced operational stability through interfacial modification by active encapsulation of perovskite solar cells. *Applied Physics Letters* **2020**, *116* (11), 113502. DOI: 10.1063/1.5144038.

(34) Yoo, S.-M.; Yoon, S. J.; Anta, J. A.; Lee, H. J.; Boix, P. P.; Mora-Seró, I. An Equivalent Circuit for Perovskite Solar Cell Bridging Sensitized to Thin Film Architectures. *Joule* **2019**, *3* (10), 2535-2549. DOI: https://doi.org/10.1016/j.joule.2019.07.014.
(35) Riquelme, A. J.; Valadez-Villalobos, K.; Boix, P. P.; Oskam, G.; Mora-Seró, I.; Anta, J. A. Understanding equivalent circuits in perovskite solar cells. Insights from drift-diffusion simulation. *Physical Chemistry Chemical Physics* **2022**, *24* (26), 15657-15671, 10.1039/D2CP01338J. DOI: 10.1039/D2CP01338J.